

Relationships between convective asymmetry, imbalance and intensity in numerically simulated tropical cyclones

By DAVID A. SCHECTER*, *NorthWest Research Associates, Boulder, CO 80301, USA*

(Manuscript received 26 November 2012; in final form 22 July 2013)

ABSTRACT

This article examines the relationships between convective asymmetry (CA), imbalance and intensity in tropical cyclones (TCs) that emerge from random winds on the periodic f -plane in a cloud-system-resolving numerical model. The model is configured with warm-rain microphysics and includes a basic parameterisation of long-wave radiation. Within the simulation set, the sea-surface temperature ranges from 26 to 32°C, and the Coriolis parameter f ranges from 10^{-5} to 10^{-4} s^{-1} . The number of TCs that develop in a simulation increases rapidly with f and ranges from 1 to 18. Taken together, the simulations provide a diverse spectrum of vortices that can be used for a meaningful statistical study.

Consistent with earlier studies, mature TCs with minimal asymmetry are found to have maximum wind speeds greater than the classic theoretical value derived by Emanuel under the assumptions of gradient-wind and hydrostatic balance. In a statistical sense, it is found that the degree of superintensity with respect to balance theory reliably decays with an increasing level of inner-core CA. It is verified that a more recent version of axisymmetric steady-state theory, revised to incorporate imbalance, provides a good approximation for the maximum (azimuthally averaged) azimuthal wind speed V_{\max} when CA is relatively weak. More notably, this theory for axisymmetric vortices maintains less than 10% error as CA becomes comparable in magnitude to the symmetric component of inner-core convection. Above a large but finite threshold of CA, axisymmetric steady-state theory generally over-predicts V_{\max} . The underachievement of TCs in this parameter regime is shown to coincide with substantial violation of the theoretical assumption of slantwise convective neutrality in the main updraft of the basic state. Of further interest, a reliable curve-fit is obtained for the anticorrelation between a *simple* measure of CA and V_{\max} normalised to an estimate of its balanced potential intensity that is based solely on environmental conditions and air–sea interaction parameters. Sensitivity of results to the surface-flux parameterisation of the numerical model is briefly discussed.

Keywords: hurricane structure, atmospheric convection, tropical meteorology, planetary vortices, modelling

1. Introduction

1.1. Background

Current understanding of tropical cyclone (TC) intensity is largely based on the influential steady-state theory of Emanuel (1986) and subsequent refinements (E86; Emanuel, 1988; Emanuel, 1995; Bister and Emanuel, 1998; Emanuel and Rotunno, 2011). Consistent with earlier studies, Emanuel's theory stresses the critical role of latent and sensible heat transfer at the air–sea interface in maintaining the circulation (cf. Malkus and Riehl, 1960; Riehl, 1963; Ooyama, 1969, 1982). The importance of this transfer is reflected in a succinct analytical expression for

the maximum azimuthal wind speed V_{\max} that increases with the magnitude of air–sea disequilibrium (see Section 3). Despite the well-recognised merits of E86, its analytical framework involves several approximations whose deficiencies are gradually coming to light [Persing and Montgomery, 2003; Montgomery et al., 2006; Smith et al., 2008; Bryan and Rotunno, 2009a,b (BR09a,b); Montgomery et al., 2010; Bryan, 2012a,b]. One such approximation is gradient-wind and hydrostatic balance. Another more basic approximation is symmetry about the central axis of rotation.

The possibility for significant violation of the balance assumption has been clearly shown in numerical simulations of axisymmetric TCs (e.g. BR09b). In these simulations, supergradient flow develops near the radius of maximum wind (RMW) and creates a condition of 'superintensity', in which V_{\max} exceeds the value given by

*Correspondence
email: schecter@nwra.com

balanced steady-state theory. Bryan and Rotunno (BR09b) recently revised the classic theoretical formula for V_{\max} to permit gradient-wind and hydrostatic imbalance, and showed that their revision accurately accounts for superintensity in many simulated hurricanes. Nevertheless, the revised theory of BR09b does not directly address the potential impact of asymmetry.

The assumption of an axisymmetric vortex is violated to some degree in all natural and realistically simulated TCs. Whether the asymmetric perturbations are associated with intrinsic fluctuations or external forcing, modelling studies typically show that non-axisymmetric TCs have weaker intensity than their axisymmetric counterparts (Frank and Ritchie, 2001; Yang et al., 2007; Riemer et al., 2010; Bryan, 2012a; Persing et al., 2013). In some cases, the weakening may be connected to the enhanced flux of low-entropy air into the convective core of the vortex (cf. Tang, 2010; Tang and Emanuel, 2010, 2012). One might also speculate that convective asymmetry (CA) weakens a TC partly by inhibiting the imbalance associated with superintensity, in loose analogy to the suppression of imbalance that is typically found upon increasing parameterised eddy-diffusivity in a numerical model (cf. Fig. 12 of BR09b).

1.2. Overview of this study

This study aims to improve current quantitative knowledge of the relationships between inner-core CA, imbalance and V_{\max} in numerically simulated TCs. To begin with, a statistical connection is sought between the degree of CA and the deviation of V_{\max} from its theoretical value derived under the assumptions of gradient-wind and hydrostatic balance. It will be shown that the degree of superintensity with respect to balance theory decreases in a fairly regular manner with increasing CA. It will be verified that the more general axisymmetric steady-state theory of Bryan and Rotunno (BR09b) largely accounts for superintensity and provides a good approximation for V_{\max} when CA is relatively weak. More surprisingly, good agreement with axisymmetric steady-state theory will be found to persist as CA becomes comparable in magnitude to the symmetric component of inner-core convection. Nevertheless, there exists a threshold of CA, above which axisymmetric steady-state theory generally over-predicts V_{\max} . The underachievement of TCs in this parameter regime will be shown to coincide with substantial violation of the theoretical assumption of slantwise convective neutrality (SCN) in the main updraft of the basic state.¹ The preceding results will be discussed further in Section 6.

On another front, a reliable curve-fit is sought for the anticorrelation between a *simple* measure of TC asymmetry and V_{\max} normalised to a classic estimate of its balanced

potential intensity (found in E86) that is based solely on environmental conditions and air-sea interaction parameters. It is worth remarking that the existence of a reliable curve-fit using a simple asymmetry variable is not a foregone conclusion, given that standard satellite-based intensity estimates involve relatively complex, multivariable algorithms (e.g. Velden et al., 2006). Here, a number of alternatives will be considered, and it will be shown that a dimensionless measure of the precipitation asymmetry works best.

The TCs considered for this study are generated by a conventional cloud-system-resolving (CSR) numerical model on the periodic f -plane. A diverse set of TCs is ensured by initialising the simulations with a pseudo-random wind field and by using a broad range of values for both the sea-surface temperature T_s and the Coriolis parameter f . In general, each simulation produces multiple TCs. The inner-core CA of an arbitrary TC may readily develop through intrinsic fluctuations. Other factors affecting CA in a multi-vortex system may include shear in the local background flow and asymmetries in the surrounding moisture fields.

It is relevant to note that similar periodic f -plane simulations have been carried out before with GCM-like models, CSR models and simple three-layer models [Held and Zhao, 2008 (HZ08); Schecter and Dunkerton, 2009; Schecter, 2010, 2011; Khairoutdinov and Emanuel, 2012 (KE12)]. The aforementioned computational studies focused on relating TC intensity, size and frequency to environmental parameters after radiative convective equilibrium (RCE) is achieved. The present simulations generally terminate before reaching RCE, but the relatively short simulation time (9–19 d) is sufficient for the TCs to reach peak intensity and settle into mature states. In a number of cases, the mature TCs slowly evolve with time. The slow evolution beneficially broadens the spectrum of states that one may include in a statistical survey.

1.3. Outline of the remaining sections

The remainder of this article is organised as follows. Section 2 provides an overview of the numerical simulations. Section 3 reviews several theoretical expressions for the maximum wind speed of an axisymmetric, steady-state TC. Section 4 discusses the primary variable that is used to measure inner-core CA in this study. Section 5 presents the statistical relationships between CA, imbalance and intensity found in the present simulation set. Section 6 summarises and discusses the results. Appendix A provides details on the numerical algorithm used to identify TCs and measure their properties in multi-vortex simulations.

2. Overview of the numerical simulations

2.1. Basic configuration of the Regional Atmospheric Modelling System

The numerical simulations are conducted with the Regional Atmospheric Modelling System (RAMS 6.0), which was originally developed at Colorado State University and is currently distributed to the public by ATMET LLC (Cotton et al., 2003). RAMS is a state-of-the-art weather research model with a variety of options for parameterising cloud microphysics, radiation, turbulent diffusivity and surface fluxes. For this study, RAMS is configured with single-moment warm-rain microphysics (Walko et al., 1995) and a long-wave radiation scheme based on the Mahrer and Pielke (1977) model. The warm-rain microphysics configuration activates only two species of hydrometeors (cloud droplets and rain), and the Mahrer–Pielke radiation scheme neglects the effects of condensate. The turbulent diffusivity is anisotropic and is obtained from a local Smagorinsky (1963) closure with Lilly (1962) and Hill (1974) modifications.

The surface-flux parameterisation in this study is simplified from the standard formulation in RAMS (Louis, 1979; Walko et al., 2000) to one closely resembling that used in the classic TC modelling study of Rotunno and Emanuel (1987; cf. Schecter, 2011). Equations of the following form are used for the surface fluxes of horizontal momentum (τ_{ux} , τ_{uy}), sensible heat (τ_θ) and moisture (τ_q)

$$\begin{aligned} \tau_{ux} &= -C_D |\mathbf{u}_+| u_{x+}, & \tau_{uy} &= -C_D |\mathbf{u}_+| u_{y+}, \\ \tau_\theta &= C_E |\mathbf{u}_+| (\theta_s - \theta_+), & \tau_q &= C_E |\mathbf{u}_+| (q_{s*} - q_+), \end{aligned} \quad (1)$$

in which $\mathbf{u} \equiv (u_x, u_y)$ is the horizontal velocity, θ is the potential temperature, and q is the water vapour mixing ratio. The variables θ_s and q_{s*} denote θ and the saturation value for q at the sea surface. The subscript ‘+’ indicates that the variable is evaluated at the first vertical grid point above sea level. The dimensionless surface-exchange coefficients are generally obtained from Deacon’s formula

$$C_D = C_E = 1.1 \times 10^{-3} + 4 \times 10^{-5} |\mathbf{u}_+|, \quad (2)$$

with $|\mathbf{u}_+|$ given in m s^{-1} . It is known today that the right-hand side (rhs) of eq. (2) is inaccurate at hurricane strength wind speeds, and that $C_D \neq C_E$ (Black et al., 2007; Bell et al., 2012). It is reasonable to expect some difference in hurricane structure when using a more realistic surface-flux parameterisation or boundary layer scheme (cf. Braun and Tao, 2000; Smith et al., 2009; Smith and Thomsen, 2010; Bryan, 2012a). A brief discussion of this issue is deferred to Section 5.4.

The simulations are conducted on a $4000 \times 4000 \text{ km}^2$ periodic f -plane. To accommodate the large horizontal

domain on a single grid, which is required (in practice) for multi-vortex simulations, the grid resolution is roughly half that which is commonly used for isolated TC simulations. The vertical grid consists of 33 elements that are continuously stretched from 200 to 900 m to 1.8 km at altitudes of 0, 10 and 23 km above sea level. The horizontal grid spacing is 3.9 km. Rayleigh damping is applied to velocity and θ perturbations at high altitudes to suppress upward propagating waves that would otherwise remain artificially trapped in the system. The damping rate increases linearly with height z , from 0 at $z = z_d$ to v_d at $z = 23 \text{ km}$ (the model top). The values of v_d range from $3.3\text{--}6.7 \times 10^{-3} \text{ s}^{-1}$, and the values of z_d are specified below.

The data points appearing in this study are derived from seven low-top (LT) and five high-top (HT) simulations. The qualifier LT/HT refers to the relatively low/high altitude of the base of the damping layer ($z_d = 16 \text{ km}$ or 20 km). A simulation is further characterised by its settings for the constant sea-surface temperature T_s and Coriolis parameter f . The values of T_s range from 26 to 32°C , and the values of f range from 1.3×10^{-5} to 10^{-4} s^{-1} . Because a low damping layer could substantially reduce the height of the TC outflow layer over a very warm ocean, only HT simulations are considered for $T_s = 32^\circ\text{C}$.

Figure 1 summarises the simulation set and provides a legend of symbols that will be used in scatter plots of the data. The shade and size of a symbol indicate the values of T_s and f . Darker symbols represent simulations with higher















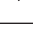



T_s ($^\circ\text{C}$)	f (10^{-5} s^{-1})	upper bound. types	symbol shade & size
26	2.5	LT, HT	 
26	10	LT, HT	 
28	3.8	LT, HT	 
28	10	LT	 
30	1.3	LT	 
30	3.8	LT	 
30	10	LT	 
32	3.8	HT	 
32	10	HT	 

Fig. 1. Summary of the simulation set, and key to the scatter plots in this article (Figs. 4a, 4b, 8b, 9, 10, 12–14). The right-most column shows the shade and relative size of symbols used for simulations with parameters given to the left.

values of T_s , and larger symbols represent simulations with higher values of f . The significance of the symbol shape (which is not necessarily a circle or diamond) depends on the particular scatter plot.

2.2. Initial conditions

In all simulations, the ambient temperature and water vapour distributions are initialised with the Jordan (1958) mean sounding for hurricane season in the West Indies. The ambient pressure field has a surface value of 1015 hPa and satisfies the hydrostatic balance equation aloft. The lower troposphere is initialised with a non-divergent, pseudo-randomly generated horizontal velocity field \mathbf{u}_r (Fig. 2). The velocity vector \mathbf{u}_r is constant with increasing height until it abruptly drops to zero at $z=6$ km. The maximum and root mean square (rms) values of $|\mathbf{u}_r|$ are 8.0 and 2.5 m s^{-1} , respectively. The power spectrum of \mathbf{u}_r is

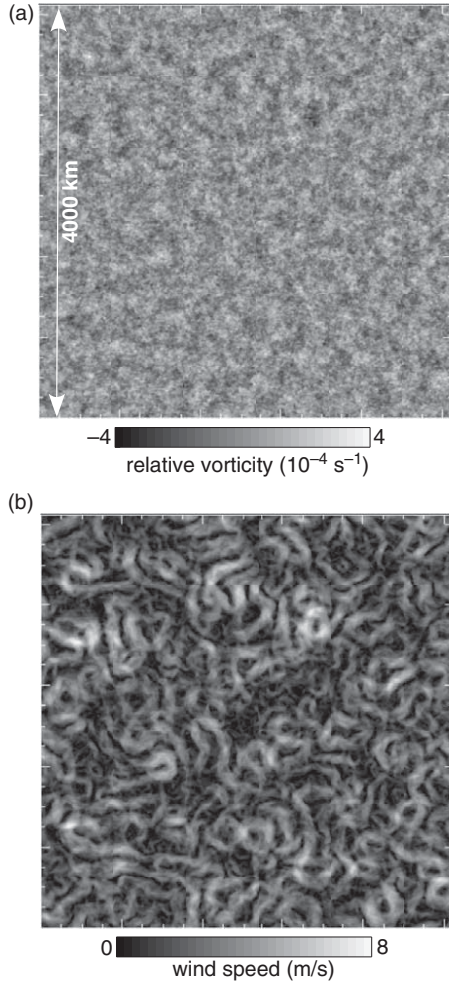


Fig. 2. The initial wind field. (a) Relative vorticity and (b) wind speed in the horizontal plane at an arbitrary altitude below $z=6$ km.

proportional to k^{-3} for horizontal wavelengths ($2\pi/k$) between 25 and 500 km, and is zero for all other wavelengths. The domain-averaged relative vorticity associated with \mathbf{u}_r is zero. The perturbation Exner function Π' (the prognostic pressure variable) is initialised to satisfy a partial differential equation (PDE) that ensures $\partial_t(\nabla_h \cdot \mathbf{u}) = 0$ at $t=0$ for the specific case in which $f=10^{-4} \text{ s}^{-1}$ (cf. Appendix B of Schecter, 2011). Here, ∇_h denotes the horizontal gradient operator. The virtual potential temperature field is slightly adjusted to ensure an initial state of hydrostatic balance. To be clear, the random velocity field is created just once, and the initial conditions for each field are the same in every simulation.²

2.3. Synopsis of the simulated TCs

Figure 3 shows selected snapshots of the z -integrated rain mass density σ in 9 out of the 12 simulations. The values of T_s , f and the time t of the snapshot are printed on each plot. In general, these snapshots depict a state of the atmosphere past the point at which the strongest TC reaches peak intensity. In some cases, the TCs have experienced partial decay and desymmetrisation (e.g. Fig. 3g). Overall, the simulation set generates a diverse spectrum of TCs with various degrees of asymmetry.

Figure 4a shows the f -dependence of the number of TCs N_v that develops in each simulation. The error bars are due to the decay of N_v with time (after reaching its peak value) in a few simulations. The rapid growth of N_v with increasing f is agreeable with empirical evidence suggesting that regions of elevated absolute vorticity are more favourable to TC development (e.g. Emanuel and Nolan, 2004; Camargo et al., 2007). It is also consistent with the RCE states of HZ08 and KE12. Note that the growth of N_v with the Coriolis parameter for $f \geq 2.5 \times 10^{-5} \text{ s}^{-1}$ seems closer to quadratic than to linear or cubic. Perhaps by coincidence, quadratic scaling would be consistent with a vortex separation length l_s proportional to the Rossby deformation radius, given that the dry static stability does not vary appreciably among the simulations. Approximate quadratic scaling (with scatter about the basic trend) might also be expected if l_s were proportional to the hypothetical RCE scale V_{th}/f (cf. HZ08; KE12; Chavas and Emanuel, 2012), in which V_{th} is the theoretical maximum wind speed of a TC derived using balance approximations in E86 [cf. eq. (7) of this article].

Figure 4b shows a scatter plot of the maximum azimuthal wind speed V_{max} against the radius of maximum wind r_{max} for mature TCs in all of the simulations. Data for both the strongest and median-strength TCs in a given simulation are shown, as these vortices will be the focus of the forthcoming statistical analysis. Different data points for the same (statistically defined) TC are taken at different

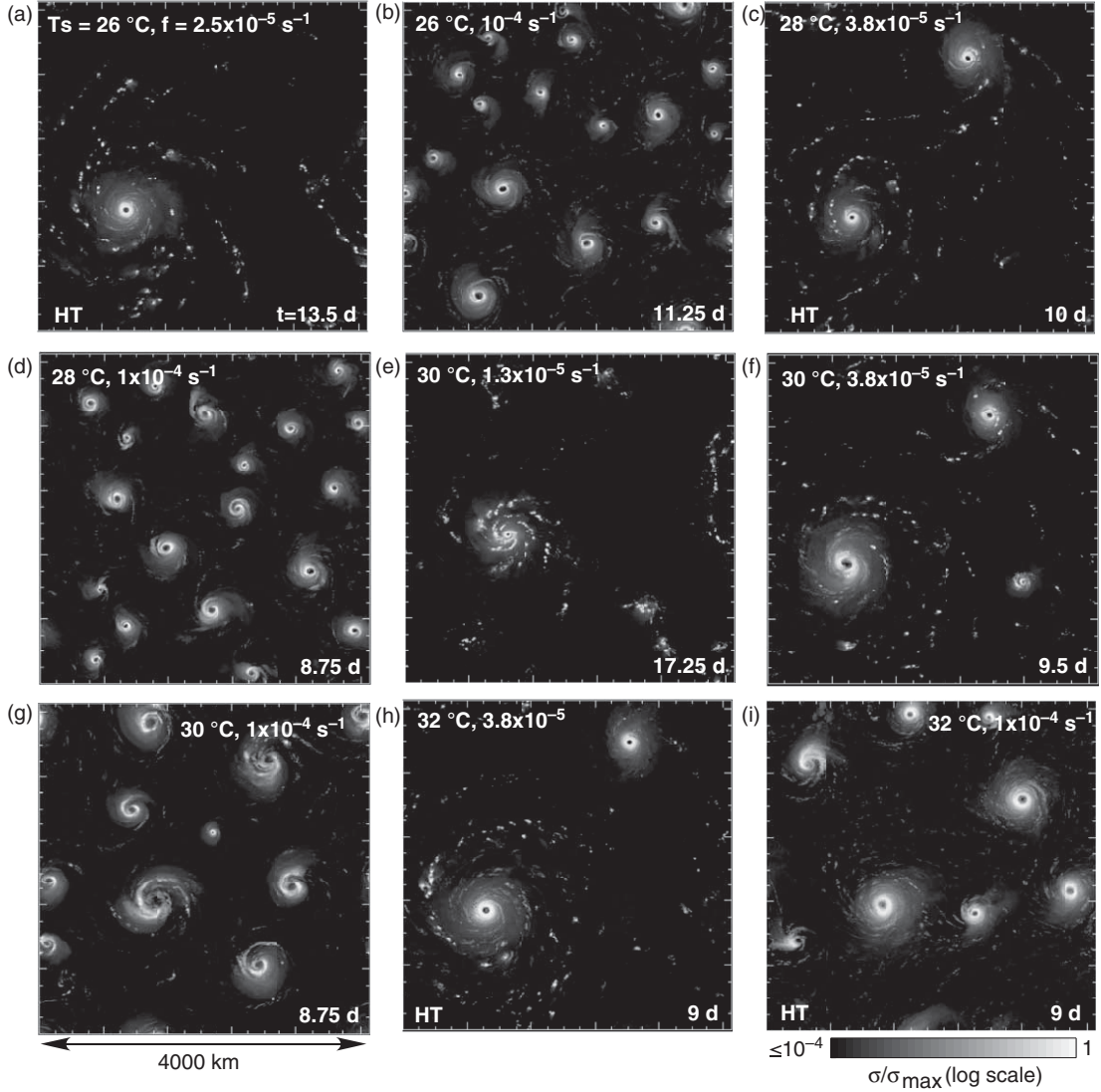


Fig. 3. (a)–(i) Snapshots of the vertically integrated rain mass density (σ) in 9 out of the 12 primary simulations used for this study. The value of σ is normalised to the maximum value in the snapshot. The sea-surface temperature T_s and Coriolis parameter f are printed on the upper edge of each panel, whereas the time of the snapshot (in days) is printed on the bottom edge. High-top simulations are labelled with an HT on the bottom-left corner.

times after peak intensity is achieved. The values for V_{\max} range from minimal hurricane strength to unnaturally high magnitudes that exceed 120 m s^{-1} . The values of r_{\max} range from 20 to 80 km and are not strongly correlated to V_{\max} . For illustrative purposes, Fig. 4c shows the location of V_{\max} in a vertical cross-section of a typical TC. Section 5.3 will address the extent to which environmental parameters control the value of V_{\max} in the present simulation set. It is worth noting that environmental control over r_{\max} seems minimal. At best, r_{\max} may have a weak positive correlation with f and a weak negative correlation with T_s at the *specific time* of peak vortex intensity.

Figure 5 shows the evolution of the maximum azimuthal wind speed V_{\max} of TCs selected from two illustrative simulations. Figure 5a corresponds to the HT simulation with $T_s = 32^\circ\text{C}$ and $f = 10^{-4} \text{ s}^{-1}$. In this case, V_{\max} exhibits considerable decay after quickly reaching its peak value.³ The decay of V_{\max} coincides with the decay of air–sea disequilibrium as the system relaxes towards RCE. Moreover, the decay of V_{\max} follows the dotted decay curve for the theoretical wind speed of a steady-state TC obtained from the instantaneous values of local parameters [eq. (5) of Section 3]. In other words, the evolution of the mature TC appears to be consistent with quasi-equilibrium

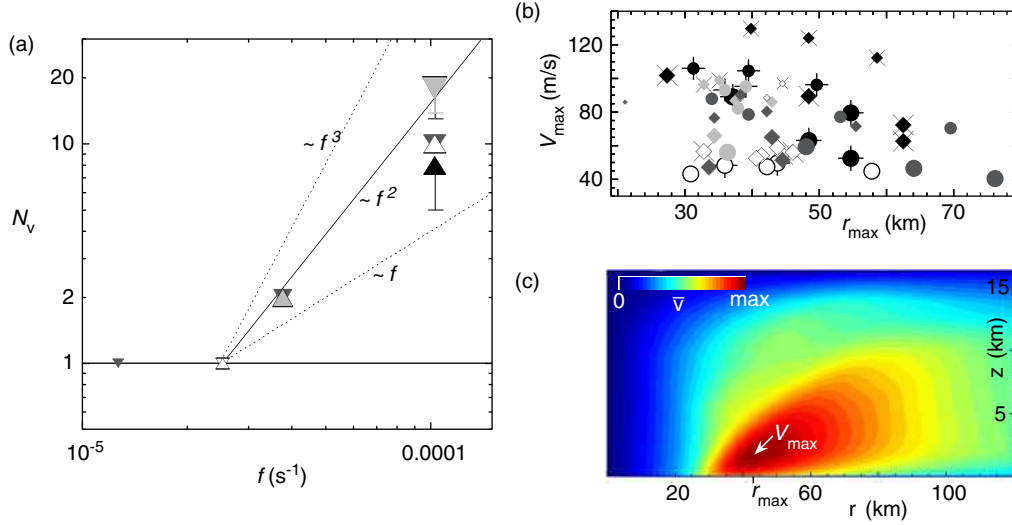


Fig. 4. (a) Number of significant vortices (N_v) versus the Coriolis parameter f . Downward and upward pointing triangles represent data from LT and HT simulations, respectively. The dotted curves show linear and cubic growth of N_v with increasing f , whereas the solid curve shows quadratic growth. (b) Scatter plot of the maximum azimuthal wind speed V_{\max} against the radius of maximum wind r_{\max} in the TCs considered for statistical analysis. The diamonds and circles respectively represent data points for the strongest and median vortices defined in Section 2.4. A '+' or 'x' behind a symbol means that the data point is taken from an HT simulation. The shading and relative size distribution of symbols in (a) and (b) are explained in Fig. 1. Each datum in (b) is a five-snapshot average, as explained in Section 4. (c) Colour contour plot of the azimuthally averaged wind speed (\bar{v}) in a typical TC, with markers at V_{\max} and r_{\max} . Specifically, this TC is from the HT simulation with $T_s = 26^\circ\text{C}$ and $f = 2.5 \times 10^{-5} \text{ s}^{-1}$.

development. Figure 5b corresponds to the HT simulation with $T_s = 26^\circ\text{C}$ and $f = 10^{-4} \text{ s}^{-1}$. In this case, the TC evolves more slowly, but again follows the basic expectations of steady-state theory after achieving peak intensity.

Note that with few exceptions, the slow evolution of V_{\max} after peak intensity coincides with slow growth of the RMW. Pertinent details on the growth rates will be discussed in Section 5.1.

2.4. Conventions for identifying and describing TCs

The vortex statistics presented in this article are obtained from snapshots taken every 6 hours (the archiving interval) in each simulation. A vortex is considered for statistical analysis only if the minimum value of its surface pressure p_s falls below a time-dependent threshold. Appendix A.1 provides details of the numerical algorithm that identifies significant vortices.

Unless stated otherwise, the central axis of the cylindrical coordinate system used to describe a TC passes through the centre of rotation \mathbf{x}_0 in the boundary layer. The radial, azimuthal and vertical coordinates are denoted r , ϕ and z , respectively. The corresponding unit vectors are given by \hat{r} , $\hat{\phi}$ and \hat{z} . The radial, azimuthal and vertical velocities are denoted u , v and w . The boundary layer is here defined as the lowest part of the troposphere, extending from the sea surface to $z = 1 \text{ km}$. The vertically averaged horizontal

velocity field in the boundary layer is denoted \mathbf{u}_0 . Appendix A.2 explains how \mathbf{x}_0 is obtained from \mathbf{u}_0 .

All fields within a TC are decomposed into azimuthal means and perturbations, henceforth denoted by overbars and primes. For example, the azimuthal velocity field is given by $v \equiv \bar{v}(r, z) + v'(r, \phi, z)$, in which $\bar{v} \equiv \int_0^{2\pi} d\phi v / 2\pi$. The value of V_{\max} is equated to the maximum of $\bar{v}(r, z)$. The radius and height at which $\bar{v} = V_{\max}$ are denoted r_{\max} and z_{\max} , respectively. The point (r_{\max}, z_{\max}) is generally within the lowest part of the eyewall updraft. In general, V_{\max} is slightly greater than the maximum value of $\bar{v}_0(r) \equiv \hat{\phi} \cdot \mathbf{u}_0$, henceforth denoted V_0 . The radius at which $\bar{v}_0 = V_0$ is denoted R_0 and may slightly differ from r_{\max} .

The statistical software developed for this study identifies the *strongest vortex* in a snapshot as that among the N_v vortices possessing the maximum of V_0 . If N_v is odd, the *median vortex* is that with the central value of V_0 . If N_v is even, the median vortex refers to an imaginary vortex whose measurement under consideration (such as an asymmetry variable) is the average between the two vortices with the two central values of V_0 . Note that the strongest and median vortices can change their identities with time. The strongest or median vortex is said to be in a *mature* state after the maximum or median value of V_0 reaches its temporal peak, and the nominal TC outflow altitude (z_0 , defined in Section 3) settles to within one vertical grid point of its final value. The remaining scatter

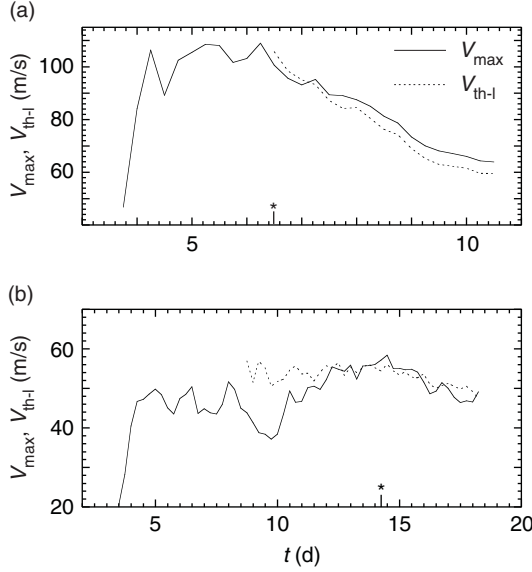


Fig. 5. Time series of the maximum wind speed (V_{\max}) of TCs selected from HT simulations with (a) $T_s = 32^\circ\text{C}$ and (b) $T_s = 26^\circ\text{C}$. In both simulations, $f = 10^{-4} \text{ s}^{-1}$. The dotted curves show the maximum wind speed given by modern axisymmetric steady-state theory [i.e., $V_{\text{th-l}}$ given by eq. (5)]. The time dependence of $V_{\text{th-l}}$ is due to changes in local conditions that determine its value. The dotted curves begin when the nominal TC outflow altitude (z_0 defined in Section 3) settles to within one vertical grid point of its final value. The asterisk in each plot marks the time at which sampling begins for obtaining scatter plot data from the depicted simulation.

plots in this article (and Fig. 4b) show data only from mature vortices. Data points from the strongest and median vortices are deemed sufficient to convey the variability of mature TC structure in a given system. The weakest TCs are not represented in the scatter plots (when $N_v \geq 3$) because it is sometimes difficult to establish their maturity or status with respect to quasi-equilibrium.

3. Theoretical wind speed formulas

Perhaps the simplest theoretical (th) expression for the square of V_{\max} pertinent to the simulations of this study is given by

$$V_{\text{th-lb}}^2 \equiv \frac{C_E}{C_D} [\bar{T}_B - T_o] (\bar{s}_{s*} - \bar{s}_+)_r, \quad (3)$$

in which the suffix ‘lb’ in the subscript of V indicates a partial dependence on *local* parameters (in contrast to ambient conditions) and limited applicability to *balanced* vortices (E95; BR09b). The first factor on the rhs of eq. (3) reflects the intensification expected from increasing the ratio of C_E to C_D . One should bear in mind, however, that the other factors may have implicit dependencies on the surface-exchange coefficients.

The middle factor on the rhs of eq. (3) accounts for the intensification of a TC by increasing the difference between the nominal cloud-base temperature \bar{T}_B and outflow temperature T_o . Here, and in all other equations of this article, the temperatures are absolute. The value of \bar{T}_B is taken to be the ϕ -averaged temperature at (r_{\max}, z_{\max}) . The value of T_o is obtained from the domain-averaged sounding (DAS) at the altitude z_o where the mixing ratio of small cloud droplets (q_c) is maximised. This practical estimate for T_o is reasonable only after the effect of deep convection on the z -maximum of q_c dominates that of shallow convection, and it may not have a straightforward generalisation to simulations with more complex microphysics. Figure 6 shows where z_o lies within the actual outflow of the strongest hurricanes in several of the simulations at hand.

The last factor on the rhs of eq. (3) accounts for the intensification of a TC by increasing a local measure of the air–sea disequilibrium. The variables \bar{s}_{s*} and \bar{s}_+ respectively represent azimuthal averages of the saturated pseudoadiabatic entropy at the sea surface and the actual pseudoadiabatic entropy at the top of the surface layer, evaluated at r_{\max} . The approximate formula for pseudoadiabatic entropy used here is given by

$$s \approx c_{pd} \ln T - R_d \ln p_d + \frac{L_0 q}{T} - q R_v \ln(\mathcal{H}), \quad (4)$$

in which c_{pd} is the isobaric specific heat of dry air, T is the absolute temperature, p_d is the pressure of dry air, q is the water vapour mixing ratio, \mathcal{H} is the relative humidity, R_d and R_v are respectively the gas constants of dry air and water vapour, and $L_0 \equiv 2.555 \times 10^6 \text{ J kg}^{-1}$ (Bryan, 2008).

The classic derivation of eq. (3) assumes that the TC is axisymmetric and time independent. More technical assumptions include the following:

A.1. the vortex satisfies gradient-wind and hydrostatic balance;

A.2. boundary layer air is conditionally neutral to slantwise displacements along angular momentum surfaces in the eyewall;

A.3. surface fluxes balance radial advection (of entropy and angular momentum) in the inflow layer at the base of the eyewall.

By now, it is well-known that $V_{\text{th-lb}}$ can severely under-predict V_{\max} largely due to violation of balance (A.1) near the RMW (Smith et al., 2008; BR09b). Permitting imbalance leads to the following more general theoretical wind speed formula [cf. eq. (23) of BR09b]

$$V_{\text{th-l}}^2 \equiv V_{\text{th-lb}}^2 + \Gamma, \quad (5)$$

in which

$$\Gamma \equiv r \bar{w} \left(\frac{\partial \bar{u}}{\partial z} - \frac{\partial \bar{w}}{\partial r} \right) \Big|_{r_{\max}, z_{\max}}. \quad (6)$$

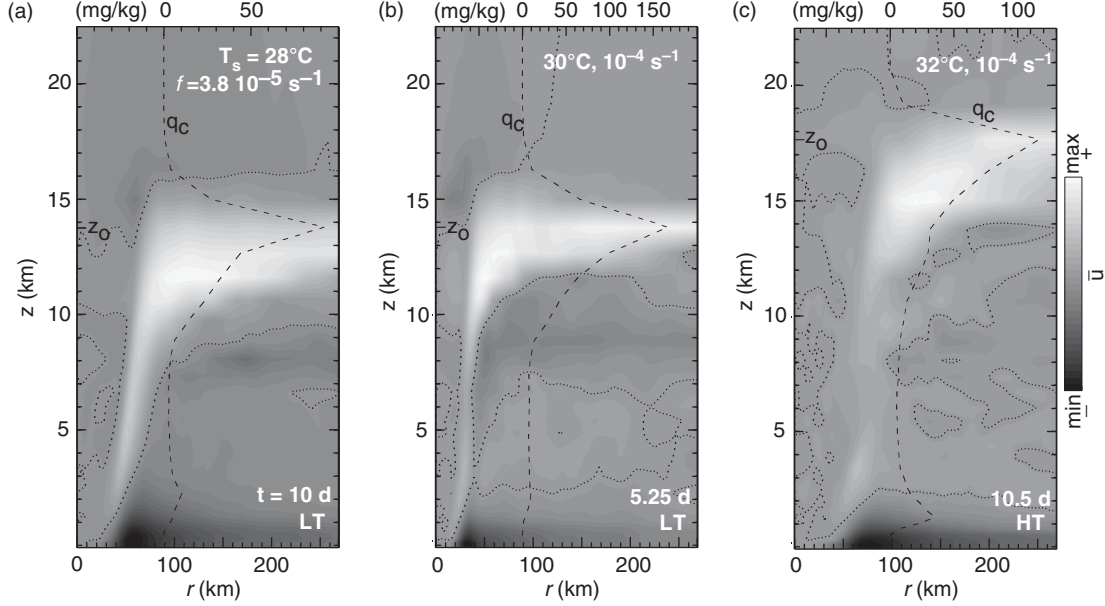


Fig. 6. Correspondence between the TC outflow region and the altitude z_0 where the horizontally averaged cloud water mixing ratio $q_c(z)$ is peaked. (a) Shaded contour plot of the radial velocity \bar{u} in the r - z plane for the strongest TC in the LT simulation with $T_s = 28^\circ\text{C}$ and $f = 3.8 \times 10^{-5} \text{ s}^{-1}$ at $t = 10 \text{ d}$. The dotted curves are zero-contours of \bar{u} ; dark/bright shades indicate inflow/outflow. A graph of q_c (dashed curve) is superposed on the contour plot of \bar{u} . The values of q_c are given on the top axis. (b) Same as (a) but for the LT simulation with $T_s = 30^\circ\text{C}$ and $f = 10^{-4} \text{ s}^{-1}$ at $t = 5.25 \text{ d}$. (c) Same as (a) but for the HT simulation with $T_s = 32^\circ\text{C}$ and $f = 10^{-4} \text{ s}^{-1}$ at $t = 10.5 \text{ d}$.

The correction due to imbalance (Γ) is simply $r\bar{w}$ times the azimuthal vorticity of the secondary circulation, evaluated at the location of maximum wind speed. Typically, the value of Γ increases with the local degree of supergradient flow (BR09b).⁴

Comparing V_{\max} to $V_{\text{th-lb}}$ or $V_{\text{th-l}}$ allows one to partially assess the consistency between a simulated TC and axisymmetric steady-state theory, with or without balance approximations. However, evaluating $V_{\text{th-lb}}$ or $V_{\text{th-l}}$ requires knowledge of secondary vortex parameters and moist-thermodynamic conditions at the base of the eyewall. In contrast, eq. (43) of E86 provides a theoretical estimate for V_{\max} that depends only on environmental conditions and air-sea interaction parameters. The E86 formula is approximately given by

$$V_{\text{th}}^2 \equiv \frac{C_E}{C_D} \frac{\epsilon L q_{s*}^a (1 - \mathcal{H}_s^a)}{1 - \frac{1}{2} \frac{C_E}{C_D} \epsilon \frac{L q_{s*}^a (1 - \mathcal{H}_s^a)}{\xi R T_s}}, \quad (7)$$

in which $L = 2.5 \times 10^6 \text{ J kg}^{-1}$ is the latent heat of vaporisation (neglecting temperature variation) and $R = 287 \text{ J kg}^{-1} \text{ K}^{-1}$ is the approximate gas constant of air. The variables q_{s*}^a and \mathcal{H}_s^a are the surface values of the saturation water-vapour mixing ratio and relative humidity

obtained from the DAS. The parameters ϵ and ξ are defined by

$$\epsilon \equiv \frac{T_B - T_o}{T_B} \text{ and } \xi = 1 - \epsilon \left(1 + \frac{L q_{s*}^a \mathcal{H}_s^a}{R T_s} \right). \quad (8)$$

The cloud-base temperature T_B is here approximated by the value of T at the lifting condensation level of an air parcel with relative humidity \mathcal{H}_s^a and temperature T_+ obtained from the DAS at the first grid point above sea level. Note that T_+ is slightly less than the sea-surface temperature T_s . The outflow temperature T_o is obtained from the DAS as described previously in connection to Fig. 6. It should be noted that eq. (7) neglects a term that appears in E86 of order $(f^2 r_o^2 / 4 \xi R T_B) V_{\text{th}}^2 \ll V_{\text{th}}^2$, in which r_o is essentially the outer radius at which the near-surface azimuthal velocity of the TC vanishes. Such neglect causes a typical error of 1% (and a maximum error of 3%) for V_{th} in the simulations under consideration, assuming hexagonal closely packed vortices to estimate r_o from N_v . It should also be emphasised that DAS quantities are substituted for ambient quantities in the practical evaluation of V_{th} . This approach seems reasonable, assuming that the inner cores of the TCs contribute little to the domain average of an arbitrary sounding variable.

4. Convective asymmetry

Several measurements of vortex asymmetry will be considered in this article. For the time being, it suffices to focus on the following measure of inner-core CA:

$$\delta\sigma \equiv \frac{\max(\sqrt{\sigma'^2})}{\max(\bar{\sigma})}. \quad (9)$$

The z -integrated rain-mass density appearing in the definition of $\delta\sigma$ was introduced earlier, and it is now precisely defined by $\sigma \equiv \int_0^{z_t} dz q_r \rho$, in which z_t is the value of z at the model top, q_r is the rain-water mixing ratio, and ρ is the mass density of the gaseous component of moist air (which adequately approximates the mass density of dry air). The maximisation operators in eq. (9) act over the radial intervals $0.5 \leq r/R_0 \leq 1.5$ or $0.5 \leq r/R_0 \leq 4$ when appearing in the numerator or denominator, respectively.⁵

For illustrative purposes, Figure 7 shows the instantaneous rain-mass field of a TC with moderate to strong asymmetry at $t = 18$ d in the HT RAMS simulation with $T_s = 26^\circ\text{C}$ and $f = 10^{-4}\text{s}^{-1}$. Figures 7a and 7b show colour contour plots of $\bar{\sigma}$ and σ , whereas Fig. 7c shows the radial distributions of $\bar{\sigma}$ and the rms of σ' taken along an azimuthal circuit. The maxima of the radial distributions in Fig. 7c are used in the denominator and numerator of the ratio defining $\delta\sigma$.

Figure 8a shows the time dependence of $\delta\sigma$ in a mature TC that was tracked during one of the simulations. Here, it is seen that $\delta\sigma$ can have order unity fluctuations over a 1-d time period. If one attempts to match the instantaneous value of $\delta\sigma$ to that of another statistic, such as the imbalance parameter used in Section 5.1 ($V_{\text{th-l}}/V_{\text{th-lb}}$, dashed curve), one can obtain very different results depending on the time t . Taking $V_{\text{th-l}}/V_{\text{th-lb}} = 1.038 \pm 0.002$, $\delta\sigma$ can be as large as 1.08 or as small as 0.45.

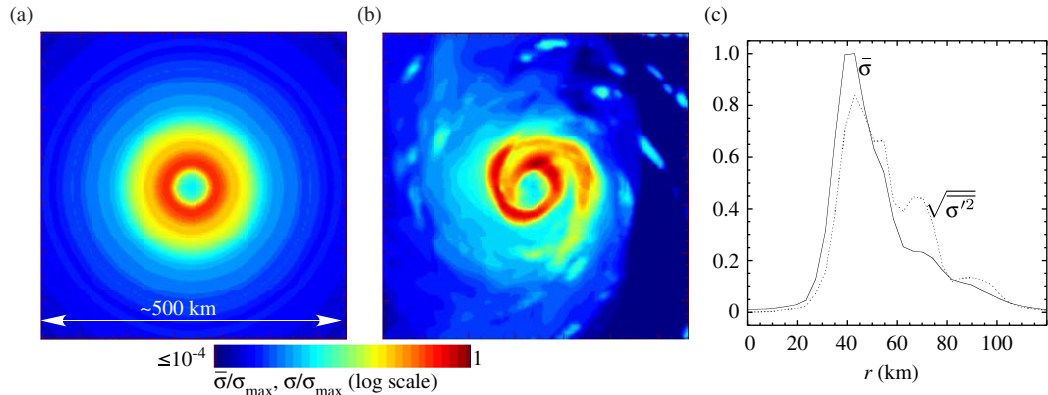


Fig. 7. Illustration of the fields used in computing the convective asymmetry variable $\delta\sigma$ for an arbitrary TC. Plots (a) and (b) are colour contour plots of the ϕ -averaged and total z -integrated rain-mass densities $\bar{\sigma}$ and σ , respectively, normalised to the maximum of σ . Plot (c) shows the radial profiles of $\bar{\sigma}$ and $\sqrt{\sigma'^2}$ normalised to $\max(\bar{\sigma})$. The RMW (in the boundary layer) is at $r = 35.2$ km.

To reduce excessive scatter associated with instantaneous measurements, the statistics plotted in this article (Figs. 4b, 8b, 9, 10, 12–14) are generally averages taken from five snapshots covering a 30-hour time window. It should be remarked that a five-snapshot-average statistic for the strongest or median vortex is not necessarily obtained from a single TC, since that vortex can change its identity over time. An illustrative comparison between averaged and unaveraged data is deferred to Section 5.3 (Fig. 13a).

It is worth noting that a positive correlation is expected between $\delta\sigma$ and other asymmetries of the secondary circulation. Figure 8b demonstrates that there is an especially strong correlation between $\delta\sigma$ and the asymmetry of core vertical kinetic energy, defined by

$$\delta KE_w \equiv \int_0^{z_d} \int_0^{3R_0} dz dr r \overline{\rho w'^2} / \int_0^{z_d} \int_0^{3R_0} dz dr r \bar{\rho} w^2. \quad (10)$$

It is also worth noting that higher grid resolution may increase the value of $\delta\sigma$ for cases in which the rain-mass asymmetry is dominated by small-scale features. Of course, all comparisons of $\delta\sigma$ made in this article are at the same resolution.

5. Statistical connections between CA, imbalance and TC Intensity

5.1. The relationship between convective asymmetry and superintensity

Having introduced a quantitative measure of CA ($\delta\sigma$), it is now possible to discuss the statistical relationship between the degree of CA and the deviation of V_{max} from its theoretical value derived under the assumptions of gradient-wind and hydrostatic balance. Figure 9a shows that V_{max} generally exceeds $V_{\text{th-lb}}$ for mature TCs with

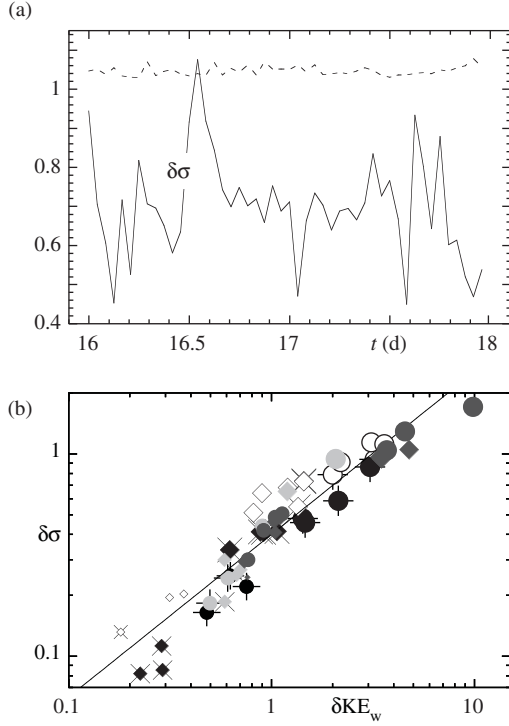


Fig. 8. (a) Time series of $\delta\sigma$ (solid curve) for a TC found in the HT simulation with $T_s = 26^\circ\text{C}$ and $f = 10^{-4} \text{ s}^{-1}$. The dashed curve shows the time series of V_{th-l}/V_{th-lb} , whose difference from unity is a dimensionless measure of imbalance. The statistical relationship between $\delta\sigma$ and V_{th-l}/V_{th-lb} is examined in Section 5.1. (b) Scatter plot of $\delta\sigma$ against the core vertical kinetic energy asymmetry δKE_w . The solid line striking through the data points is a power-law curve-fit. The symbols are the same as in Fig. 4b.

$\delta\sigma < 1$. Furthermore, the degree of superintensity ($V_{\max}/V_{th-lb} - 1$) is seen to decay in a fairly regular manner with increasing $\delta\sigma$. A few simulations have data points that fall significantly below the main (top) decay curve. Nevertheless, when the lower simulations are considered separately, they too show that superintensity decays with increasing $\delta\sigma$.⁶

Figure 9b provides evidence that superintensity is largely due to imbalance in the simulated TCs. Specifically, Fig. 9b shows that in the domain of superintense vortices, V_{\max} is generally within 10% of the value given by axisymmetric steady-state theory generalised to include imbalance (V_{th-l}). Interestingly, this high degree of accuracy persists for values of $\delta\sigma$ up to unity.

Taken together, Figs. 9a and 9b suggest that the decay of superintensity with increasing $\delta\sigma$ coincides with the decay of imbalance. Figure 10 verifies the implied anticorrelation between $\delta\sigma$ and imbalance, measured by the ratio $V_{th-l}/V_{th-lb} \equiv \sqrt{1 + \Gamma/V_{th-lb}^2}$. While a causal connection cannot be inferred from an anticorrelation, the statistical

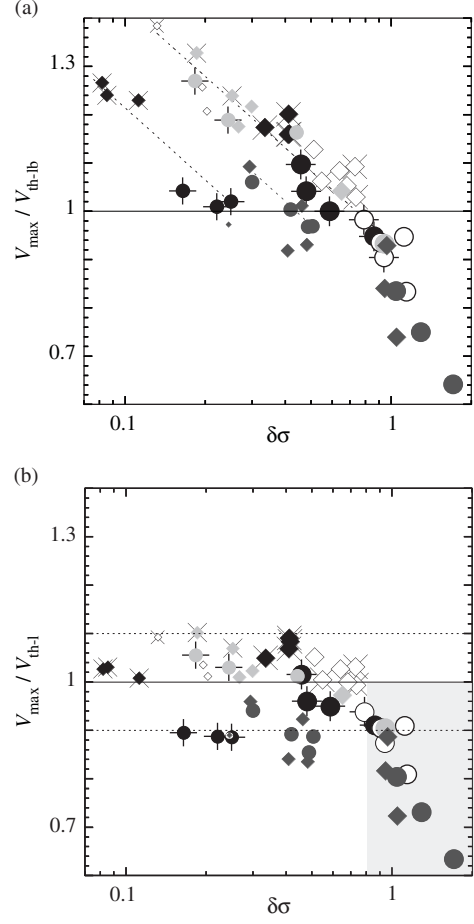


Fig. 9. Maximum wind speed V_{\max} divided by one of two theoretical values vs. the inner-core convective asymmetry variable $\delta\sigma$. The theoretical wind speed V_{th-lb} in (a) assumes gradient-wind and hydrostatic balance. The theoretical wind speed V_{th-l} in (b) accounts for imbalance. Data are shown for the median and strongest vortices (after achieving peak intensity) in all simulations. The symbols are the same as in Fig. 4b (cf. Fig. 1). The top dotted line in (a) shows the decay trend for $\delta\sigma < 1$ in most simulations. The lower dotted lines in (a) show the decay trends for two simulations that fall below the main curve. The solid horizontal line in both (a) and (b) corresponds to perfect agreement with theory. The dotted lines in (b) correspond to 10% positive and negative deviations from theory. The lightly shaded region in the lower right corner of (b) shows where $\delta\sigma \geq 0.8$ and only underachieving vortices with $V_{\max} < V_{th-l}$ exist.

decay of V_{th-l}/V_{th-lb} with increasing CA might lead one to speculate that elevated CA acts to inhibit imbalance (i.e. supergradient flow). The merit of this speculation will be assessed in Section 6, after further examination of the data.

Note that a few of the TCs with $\delta\sigma < 1$ in Fig. 9b are anomalous in that $V_{\max}/V_{th-l} < 0.9$. Unsurprisingly, the aberrant TCs belong to the same simulations whose data points fall below the main decay curve in Fig. 9a. These simulations have additional abnormalities worth

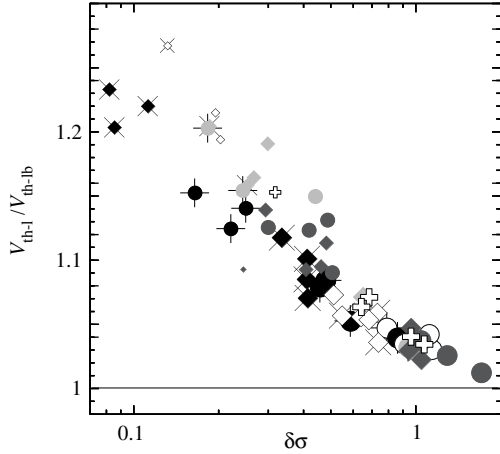


Fig. 10. The ratio of theoretical wind speeds for unbalanced and balanced TCs (V_{th-1}/V_{th-lb}) vs. $\delta\sigma$. The symbols are generally the same as in Fig. 4b. However, the white plus-marks are from additional simulations with capped surface-exchange coefficients, $T_s = 26^\circ\text{C}$, and either $f = 2.5 \times 10^{-5} \text{ s}^{-1}$ (small symbol) or $f = 10^{-4} \text{ s}^{-1}$ (large symbols).

mentioning. One of the simulations at issue is the LT experiment with $T_s = 30^\circ\text{C}$ and $f = 1.3 \times 10^{-5} \text{ s}^{-1}$. In this case, the RMW of the sole TC is exceptionally small (Fig. 4b, far left), and inadequate grid resolution is a conceivable source of error. In the other two simulations, the RMWs of the mature TCs have abnormally fast growth rates. In other words, these simulations seem to violate the steady-state assumption more so than others. For the abnormal HT simulation with $T_s = 32^\circ\text{C}$ and $f = 3.8 \times 10^{-5} \text{ s}^{-1}$, the RMW growth rate (averaged over all TCs) during the last 2 days of simulation time is 6.8 km d^{-1} . For the abnormal LT simulation with $T_s = 30^\circ\text{C}$ and $f = 3.8 \times 10^{-5} \text{ s}^{-1}$, the growth rate is 13.7 km d^{-1} . For all other simulations, the RMW growth rate has an average value of 2.2 km d^{-1} and a maximum value of 3.9 km d^{-1} .

5.2. An apparent asymmetry threshold for the integrity of axisymmetric steady-state theory

The continued decay of V_{\max}/V_{th-lb} with increasing $\delta\sigma$ beyond unity (Fig. 9a) is not attributable to a further decline of imbalance, but appears to be connected in part to the breakdown of SCN in the main updraft of the basic state.¹ Figure 11 compares the ϕ -averaged structure of a TC with $\delta\sigma = 0.13$ and $V_{\max}/V_{th-1} = 1.09$ to that of an underachieving TC with $\delta\sigma = 1.4$ and $V_{\max}/V_{th-1} = 0.66$. Each panel shows superposed contour plots of absolute angular momentum $M \equiv r\bar{v} + fr^2/2$, saturated pseudoadiabatic entropy \bar{s}_* and vertical velocity \bar{w} . The congruence of M and \bar{s}_* contours in the eyewall updraft of the TC with $\delta\sigma = 0.13$ is tantamount to SCN, and it is typical of mature

TCs that have low to moderate CA. The incongruence of M and \bar{s}_* contours in the underachieving TC with $\delta\sigma = 1.4$ indicates the violation of SCN. One reasonable measure for the violation of SCN is given by $\varepsilon_{\text{SCN}} \equiv (\bar{s}_{* \max} - \bar{s}_{*6})/\bar{s}_{* \max}$, in which $\bar{s}_{* \max}$ is \bar{s}_* evaluated at (r_{\max}, z_{\max}) and \bar{s}_{*6} is \bar{s}_* evaluated at $z = 6 \text{ km}$ on the M contour passing through (r_{\max}, z_{\max}) . The value of ε_{SCN} for the underachieving TC in Fig. 11b is 30 times greater than its value for the nearly symmetric TC in Fig. 11a.

While seen here only for a few TCs, it seems plausible that $\delta\sigma > 1$ should more generally correspond to the breakdown of SCN, which is based on the supposition of purely axisymmetric, time-independent moist-convection.

5.3. Predicting wind speed from environmental conditions and the degree of asymmetry

As noted earlier, E86 provides an estimate for TC intensity [V_{th} given by eq. (7)] that depends only on environmental conditions and the ratio C_E/C_D (which here equals 1). It is of interest to investigate whether or not the deviation of V_{\max} from V_{th} is reliably predicted by the degree of vortex asymmetry in the present simulation set. The analysis shown here includes all TCs in Fig. 9, but similar results are found using only those with $|V_{\max}/V_{th-1} - 1| \leq 0.1$.

Figure 12a demonstrates that the deviation of V_{\max}/V_{th} from unity is predicted fairly well by the value of $\delta\sigma$. The goodness of this predictor may be compared to that of other asymmetry variables. Figures 12b–d show scatter plots of V_{\max}/V_{th} against the following measures of inner-core asymmetry:

$$\delta w \equiv \frac{\max(\sqrt{w_0^2})}{\max(\bar{w}_0)}, \quad \delta u \equiv \frac{\max(\sqrt{u_0^2})}{\max(|\bar{u}_0|)}, \quad \text{and Tilt} \equiv \frac{2\delta x_{12}}{(R_1 + R_2)}. \quad (11)$$

The low-level updraft asymmetry δw involves the vertical velocity $w_0(r, \phi)$ at $z = 1 \text{ km}$. The radial inflow asymmetry δu involves the radial velocity $u_0(r, \phi)$ defined as the vertical average of u between the sea surface and $z = 1 \text{ km}$. The Tilt is generally the horizontal distance δx_{12} between rotational centres \mathbf{x}_1 at $p_1 = 850 \text{ hPa}$ and \mathbf{x}_2 at $p_2 = 200 \text{ hPa}$, divided by the mean RMW at these pressure levels (the mean of R_n , $n \in \{1, 2\}$). The maximisation operators in eq. (11) have the same meaning as in the definition of $\delta\sigma$ [eq. (9)]. The operands are generally maximised in the vicinity of the eyewall, but they are not necessarily maximised at the same radius. Appendix A provides some technical details on the computations of u_0 , \mathbf{x}_n and R_n .

Visual inspection of Fig. 12 suggests that $\delta\sigma$ is a better predictor of V_{\max}/V_{th} than the alternatives given above. To state this quantitatively, the decay of V_{\max}/V_{th} with each asymmetry variable is fit to a power-law using the method of least-squares. Each curve-fit is printed on the corresponding graph. The accuracy of one fit relative to

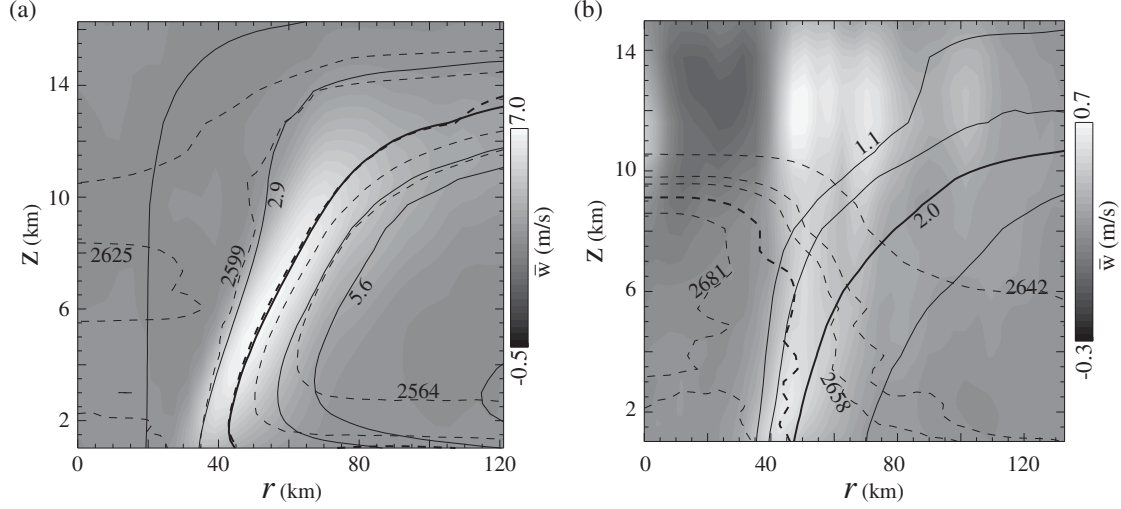


Fig. 11. Mean structure above the inflow layer for simulated TCs with (a) $\delta\sigma=0.13$ and (b) $\delta\sigma=1.4$. The solid and dashed curves are contours of constant angular momentum (M) and saturation entropy (\bar{s}_s), sparsely labelled in units of $10^6 \text{ m}^2 \text{ s}^{-1}$ and $\text{J kg}^{-1} \text{ K}^{-1}$, respectively. The relatively thick contours pass through the location of V_{\max} . The shading shows the azimuthally averaged vertical velocity \bar{w} . The TC in (a) is the sole vortex at the end of the HT simulation with $T_s=26^\circ\text{C}$ and $f=2.5 \times 10^{-5} \text{ s}^{-1}$. The TC in (b) is one of the median vortices near the end of the LT simulation with $T_s=30^\circ\text{C}$ and $f=10^{-4} \text{ s}^{-1}$. In both cases, the profiles are averages over five snapshots taken 6 hours apart.

another is here assessed by comparing the computed values of

$$Q \equiv \sqrt{\frac{\sum_i (y_i - y_{fi})^2}{\sum_i (y_i - \bar{y})^2}}, \quad (12)$$

in which y_i and y_{fi} are the logarithms of the actual and fit values of V_{\max}/V_{th} at the i -th data point, \bar{y} is the mean of y_i , and the sums are over all data points. The denominator in eq. (12) does not vary in this analysis. The value of Q is generally between 0 and 1, with 0 indicating a perfect fit and 1 indicating an rms deviation of y_i from the curve-fit equal to the standard deviation of y_i from its mean.

It is found that $Q_{\delta\sigma}=0.43$, $Q_{\delta w}=0.61$, $Q_{\delta u}=0.72$ and $Q_{\text{Tilt}}=0.78$, in which the subscript indicates the asymmetry used as the predictor of V_{\max}/V_{th} . The inferior predicting value of Tilt seems reasonable given that the pressure levels of \mathbf{x}_1 and \mathbf{x}_2 are somewhat arbitrary, and δx_{12} does not usually exceed a few grid increments in the simulation set at hand. It is not as obvious to the author why δw and δu are inferior to $\delta\sigma$, but this result may deserve further study if found to be common in future computational experiments and observational analyses.⁷

Of course, one cannot claim that $\delta\sigma$ is the best of all possible predictors for V_{\max}/V_{th} . Not only does $\delta\sigma$ contain

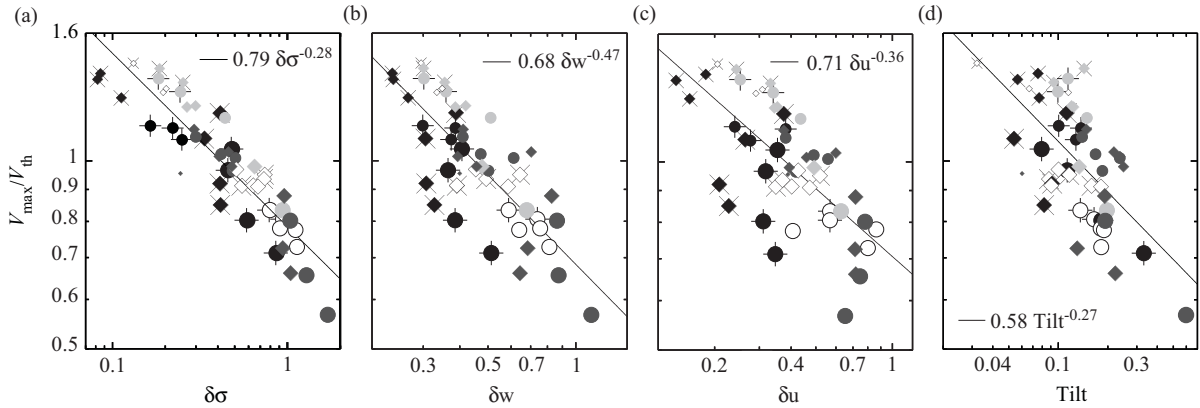


Fig. 12. Comparison of the reliability of different asymmetry variables for predicting V_{\max}/V_{th} . (a–d) Scatter plots of V_{\max}/V_{th} against (a) $\delta\sigma$, (b) δw , (c) δu and (d) Tilt. The rain-mass asymmetry $\delta\sigma$ is the most reliable predictor of those considered here. The symbols are the same as in Fig. 4b.

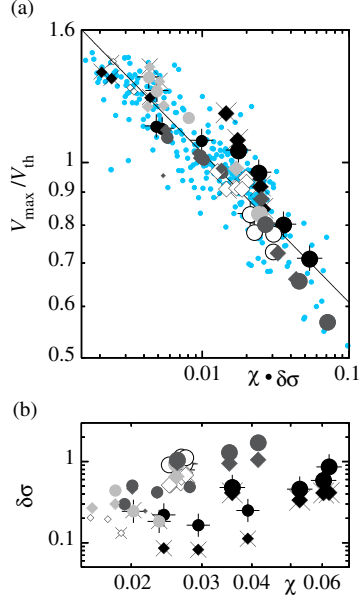


Fig. 13. (a) Non-dimensional wind speed V_{\max}/V_{th} vs. the product of the lower-middle tropospheric moist-entropy deficit χ and the convective asymmetry variable $\delta\sigma$. The curve-fit (solid line) is given by $V_{\max}/V_{\text{th}} = 0.36(\chi\delta\sigma)^{-0.23}$. (b) Scatter plot of $\delta\sigma$ against χ . The symbols are generally the same as in Fig. 4b, but the small blue dots in (a) show instantaneous measurements as opposed to averages taken over five snapshots (white, black and grey symbols).

incomplete information on the structural asymmetry of the vortex, but environmental factors could affect the impact of asymmetric perturbations on vortex intensity. One conceivable hybrid predictor is $\delta\sigma$ multiplied by the following dimensionless measure of the lower-middle tropospheric moist-entropy deficit⁸

$$\chi \equiv \frac{s_{m*} - s_m}{s_{m*}}. \quad (13)$$

Here, s_m and s_{m*} are actual and saturation values of the pseudoadiabatic entropy of the DAS at $p=600$ hPa. Figure 13a shows a scatter plot of V_{\max}/V_{th} against $\chi\delta\sigma$. The power-law curve-fit for the anticorrelation has a normalised error of $Q_{\chi\delta\sigma} = 0.37$, which is a small but notable improvement over $Q_{\delta\sigma} = 0.43$. It has been found that $\chi\delta w$, $\chi\delta u$ and χTilt are also better power-law predictors of V_{\max}/V_{th} than their bare counterparts (compare $Q_{\chi\delta w} = 0.41$, $Q_{\chi\delta u} = 0.40$ and $Q_{\chi\text{Tilt}} = 0.64$ to the Q values given in the preceding paragraph). Typical improvement in the predictive value of an asymmetry variable by factoring in χ could be accidental, but it seems agreeable with the general notion that the flux of low-entropy air into the convective core of the storm factors into the detrimental impact of asymmetric perturbations on TC intensity.

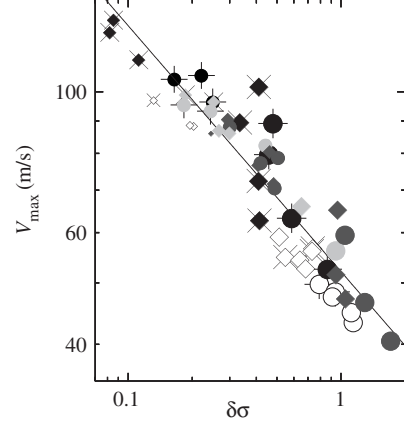


Fig. 14. Dimensional wind speed V_{\max} versus $\delta\sigma$. The curve-fit (solid line) is given by $V_{\max} = 52\delta\sigma^{-0.39}$ in units of m s^{-1} . The symbols are the same as in Fig. 4b.

Figure 14 shows that in addition to its anticorrelation with V_{\max}/V_{th} , the rain-mass asymmetry $\delta\sigma$ has a fairly strong anticorrelation with the dimensional wind speed V_{\max} in the simulation set at hand. One might liberally combine the curve-fit equation for V_{\max}/V_{th} against $\delta\sigma$ (or $\chi\delta\sigma$) with the curve-fit equation for V_{\max} against $\delta\sigma$ to obtain an ad hoc equation for V_{\max} that depends only on environmental conditions and air–sea interaction parameters. However, it is the author’s opinion that the effort to accurately eliminate asymmetry from the V_{\max} equation under general circumstances is best deferred until future theoretical work provides more guidance.

A few brief remarks are in order before proceeding to the next section. First note that the power-law curve-fits in Figs. 12–14 are not supposed to apply outside the finite bounds of asymmetry (and χ) in the present data set. This is seen clearly from the unphysical divergence of V_{\max} predicted by the curve-fits as asymmetry tends to zero. Note also that while data averaged over five snapshots is used here to quantify the decay of V_{\max}/V_{th} with increasing asymmetry, the instantaneous data points (e.g. the small blue dots in Fig. 13a) typically do not stray too far from the averaged data points. A few exceptions are seen in Fig. 13a, as one might have anticipated from the discussion of Section 4 in connection to Fig. 8a. Note finally that while elevated levels of χ may be one cause for elevated levels of $\delta\sigma$, the two quantities are not strongly correlated in the present computational data set (Fig. 13b).

5.4. Comment on the surface-flux parameterisation

The anticorrelation between V_{\max} and $\delta\sigma$ in Fig. 14 suggests that greater imbalance at low values of $\delta\sigma$ coincides with greater values of C_D and C_E [see eq. (2)]. One might reasonably suspect that such intensification of

the surface-exchange coefficients influences the degree of supergradient flow. A comprehensive surface-flux sensitivity test is not presented in this article. However, the author has briefly examined the consequence of capping the values of C_D and C_E in the two HT simulations with $T_s = 26^\circ\text{C}$, by letting $|\mathbf{u}_+| \rightarrow \min(|\mathbf{u}_+|, 30 \text{ m s}^{-1})$ in eq. (2). In neither case does V_{\max} change by more than 9%. For the simulation in which $f = 10^{-4} \text{ s}^{-1}$, the imbalance measured by $V_{\text{th-l}}/V_{\text{th-lb}}$ changes by an average magnitude of 10^{-2} . For the simulation in which $f = 2.5 \times 10^{-5} \text{ s}^{-1}$, $V_{\text{th-l}}/V_{\text{th-lb}}$ decreases by 0.11. The greater reduction of imbalance in the latter case coincides with greater fractional growth of $\delta\sigma$. Returning to Fig. 10 of Section 5.1, it is seen that the anticorrelation between imbalance and $\delta\sigma$ in the capped simulations (white plus-marks) quantitatively agrees with that found in the uncapped simulations. This result lends credence to the hypothesis that the basic anticorrelation between imbalance at the location of V_{\max} and inner-core CA is not a peculiar artefact of the Deacon-type surface-flux parameterisation used for this study.

6. Summary and concluding remarks

In summary, this article examined the statistical relationships between inner-core CA, imbalance and TC intensity in a CSR model on the periodic f -plane. The CSR model was configured with warm-rain microphysics, a traditional parameterisation of surface fluxes [eqs. (1) and (2)], Smagorinsky-type eddy-diffusivity, and a simplified long-wave radiation scheme. The number of TCs generated in a simulation was found to increase rapidly with f , and ranged from 1 to 18. The statistics were obtained after the TCs achieved peak intensity.

The degree of CA was quantified by the parameter $\delta\sigma$ [eq. (9)], which is a direct measure of the rain-mass asymmetry in the vicinity of the eyewall, and an indirect measure of asymmetry in the core vertical kinetic energy distribution (Fig. 8b). The statistical analysis showed that the degree of superintensity with respect to balance theory tends to decay with increasing $\delta\sigma$ (Fig. 9a). Moreover, it was shown that the degree of imbalance at the location of maximum wind speed reliably decays with increasing $\delta\sigma$ (Fig. 10).

A definitive interpretation of the structural anticorrelation between inner-core CA and imbalance cannot be established without further theoretical and experimental investigation. On the one hand, it seems plausible that inner-core CA would act to weaken and smooth the φ -averaged secondary circulation at (r_{\max}, z_{\max}) in such a way that reduces the pertinent measure of imbalance [Γ in eq. (6) divided by $V_{\text{th-lb}}^2$]. On the other hand, inner-core CA is statistically related to other variables that could independently influence the degree of imbalance. For example,

one must consider the anticorrelation between inner-core CA and the dimensional maximum wind speed V_{\max} (Fig. 14). Notably, the weakening of TC wind speed decreases the surface drag coefficient C_D (not to mention $C_D|\mathbf{u}_+|$) in the CSR model used for this study. It seems reasonable to speculate that the reduction of surface drag attending the growth of inner-core CA contributes significantly to the decay of imbalance shown by Fig. 10 (cf. Montgomery et al., 2010; Bryan, 2012a).

This article also verified that the generalised axisymmetric steady-state theory of Bryan and Rotunno (BR09b) largely accounts for superintensity in simulated TCs, and provides a good approximation for V_{\max} in the parameter regime where $\delta\sigma \ll 1$. More surprisingly, it was found that the wind speed given by this theory for *axisymmetric* vortices stays within 10% of V_{\max} for values of $\delta\sigma$ up to 1, provided that quasi-equilibrium is not strongly violated. (See Fig. 9b and the connected discussion.) It is worth noting that $\delta\sigma$ of order unity corresponds to an asymmetry of core vertical kinetic energy (δKE_w) of the same general magnitude. Furthermore, values of $\delta\sigma$ between 0.5 and 1 often coincide with radial inflow and/or low-level updraft asymmetries (δu and/or δw) in the same range.

Only a few data points were considered with $\delta\sigma > 1$. Here, it was found that axisymmetric steady-state theory substantially over-predicts V_{\max} . The underachievement of TCs in this parameter regime was shown to coincide with substantial violation of the theoretical assumption of SCN in the main updraft of the basic state (see Fig. 11b). It was speculated that $\delta\sigma > 1$ should more generally correspond to the breakdown of SCN, which is based on the supposition of purely axisymmetric, time-independent moist-convection.¹

Furthermore, it was shown that the value of $\delta\sigma$ is a relatively good statistical predictor of the deviation of V_{\max} from the theoretical estimate of E86 (V_{th}) that depends only on environmental conditions and air-sea interaction parameters. The superior predictive value of $\delta\sigma$ was determined upon comparison to several other measures of vortex asymmetry (Fig. 12). Interestingly, the asymmetry variables became better statistical predictors of V_{\max}/V_{th} (in this data set) when multiplied by a dimensionless measure χ of the lower-middle tropospheric moist-entropy deficit. This result could be accidental, but it seems agreeable with the general notion that the flux of low-entropy air into the convective core of the storm factors into the detrimental impact of asymmetric perturbations on TC intensity.

It is reasonable to assume that changing the grid resolution, surface-flux parameterisation, microphysics parameterisation, turbulent diffusion scheme or radiation scheme would change details of the simulations considered in this article. For example, changing the computational configuration may well change the precise magnitudes of inner-core CA and imbalance in any given TC. However,

one might hypothesise that the statistical relationship between these two quantities in a large set of reconfigured simulations would be similar to that found here. One might further hypothesise that the reconfigured simulations would exhibit the same threshold ($\delta\sigma \approx 1$) of applicability for axisymmetric steady-state theory, and a similar statistical dependence of V_{\max}/V_{th} on $\delta\sigma$ or one of its surrogates. Of course, with more realistic microphysics it might be necessary to generalise the definitions of $\delta\sigma$ and V_{th} to account for ice. Regardless, the results presented in this article provide a reference point for future investigations.

7. Acknowledgments

The author thanks two anonymous reviewers for their constructive criticism of the original manuscript which led to numerous improvements in the final submission. This work was supported by two NSF grants: AGS-0750660 and AGS-1101713. The HT simulations were partly carried out on the Bluefire and Yellowstone supercomputers at the National Centre for Atmospheric Research (Boulder, CO, USA) and on the Gordon supercomputer at the San Diego Supercomputing Centre (San Diego, CA, USA).

Appendix A

A.1. Vortex identification

To obtain vortex statistics requires a method for identifying distinct TCs and locating their centres. The present method first searches for the maximum value of the surface pressure deficit, $\hat{p}_s \equiv \langle p_s \rangle_d - p_s$, in which $\langle \dots \rangle_d$ is the horizontal domain average of the bracketed quantity. A recursive algorithm then finds an undetermined number (N_v) of distinct areas $A_{0,\alpha}$ in the horizontal plane where $\hat{p}_s \geq \kappa \max(\hat{p}_s)$, in which $0 < \kappa < 1$ and $\alpha = 1, 2, \dots, N_v$ is the vortex identification number. With a judicious choice of κ (usually between 0.3 and 0.7), the area $A_{0,\alpha}$ is generally associated with a distinct TC. With higher grid resolution, the preceding algorithm may need to be refined so as not to mistake enhanced mesovortices as additional TCs. For this simulation set, it seems to work well.

Note that the subscript ‘ α ’ used throughout this appendix is dropped for simplicity from all pertinent variables in the main text, where the context generally makes the use of α unnecessary.

A.2. Centre finding algorithm

The centre of rotation in the boundary layer of the vortex represented by α is obtained by a straightforward procedure. First, the horizontal velocity field is vertically averaged over the interval $0 < z < 1$ km. The result is

denoted by \mathbf{u}_0 . Second, $A_{0,\alpha}$ is redefined to exclude the subspace where \hat{p}_s is less than one-half its local maximum. A polar coordinate system (r, φ) is then established at each grid point \mathbf{x} in $A_{0,\alpha}$, and the φ -averaged azimuthal velocity field $[\bar{v}_x(r)]$ is obtained for that system from \mathbf{u}_0 . The centre of rotation $\mathbf{x}_{0,\alpha}$ is defined to be the coordinate centre \mathbf{x} in $A_{0,\alpha}$ that maximises the radial maximum of $\bar{v}_x(r)$. For $\mathbf{x} = \mathbf{x}_{0,\alpha}$, let $\bar{v}_x \equiv \bar{v}_{0,\alpha}$. The radius r at which $\bar{v}_{0,\alpha}$ is maximised (i.e. the RMW in the boundary layer of the TC) is denoted by $R_{0,\alpha}$.

To measure Tilt, the rotational centre is required at some low altitude (level 1) and some high altitude (level 2). Under ordinary circumstances, these levels correspond to pressure isosurfaces with $p_1 = 850$ hPa and $p_2 = 200$ hPa. If a TC is sufficiently intense, the p_1 -isosurface can penetrate the boundary layer and even ‘dip below’ the sea surface. In regions where $p_+ < p_1$, the fields of level 1 are evaluated at the first grid point above sea level. Such unnatural regions appear only for a brief time (near peak vortex intensity) in the HT simulations with $T_s = 32^\circ\text{C}$.

The searches for rotational centres on levels 1 and 2 are confined to the areas $A_{1,\alpha}$ and $A_{2,\alpha}$. The area $A_{n,\alpha}$ ($n \in \{1, 2\}$) is initially defined as a square box of length $2\beta R_{0,\alpha}$ centered about $\mathbf{x}_{0,\alpha}$, in which β is usually 3. The area $A_{n,\alpha}$ is then redefined as the subspace within $A_{n,\alpha}$ that covers $A_{n-1,\alpha}$ and any additional region where the geopotential deficit $\hat{\phi}_n$ exceeds one-half its maximum in $A_{n,\alpha}$. By definition $\hat{\phi}_n \equiv \langle \phi_n \rangle_d - \phi_n$, in which ϕ_n is the geopotential on level n . The centre of rotation $\mathbf{x}_{n,\alpha}$ in $A_{n,\alpha}$ is found as for level 0 (the boundary layer) using the horizontal velocity field \mathbf{u}_n on level n instead of \mathbf{u}_0 . Note that $A_{1,\alpha}$ is redefined before $A_{2,\alpha}$. Note also that if the maximum of $\hat{\phi}_n$ in $A_{n,\alpha}$ is negative, different rules are used to reduce $A_{n,\alpha}$ prior to searching for $\mathbf{x}_{n,\alpha}$. Such cases are uncommon and not worth a detailed discussion. Occasionally, the reduction of $A_{2,\alpha}$ leaves a few small fragments outside the central region of interest.

Figure A.1 shows the areas $A_{0,\alpha}$, $A_{1,\alpha}$ and $A_{2,\alpha}$ that are used to search for the height-dependent rotational centres of 10 TCs at $t = 8.75$ d in the LT RAMS simulation with $T_s = 30^\circ\text{C}$ and $f = 10^{-4} \text{ s}^{-1}$. In this example, $\kappa = 0.5$ and $\beta = 3$.

A.3. Note on the horizontal velocity fields used to evaluate asymmetry

Before calculating the radial inflow asymmetry of a TC (δu), the regional mean is subtracted from the horizontal velocity field \mathbf{u}_0 of the boundary layer. The regional mean is here defined as the areal average over a $1000 \times 1000 \text{ km}^2$ box centred on $\mathbf{x}_{0,\alpha}$. The magnitude of the regional mean of \mathbf{u}_0 rarely exceeds a few metres per second.

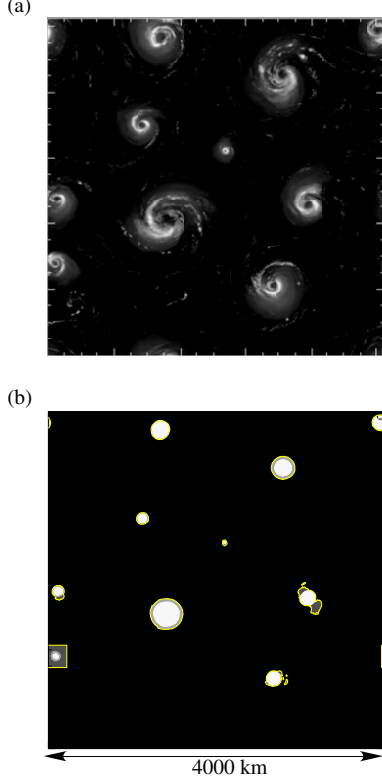


Fig. A.1. (a) Reference plot of σ showing $N_v = 10$ significant vortices at $t = 8.75$ d in the LT RAMS simulation with $T_s = 30^\circ\text{C}$ and $f = 10^{-4} \text{ s}^{-1}$. The greyscale is the same as in Fig. 3. (b) Illustration of the areas used to search for the height-dependent vortex centres. $A_{0,\alpha}$ covers the white region in the vicinity of a particular vortex; $A_{1,\alpha}$ covers the white and light grey regions; $A_{2,\alpha}$ covers the white, light grey and dark grey regions. The boundaries of $A_{2,\alpha}$ are traced with yellow contours to aid the eye. In general, $A_{0,\alpha} \subseteq A_{1,\alpha} \subseteq A_{2,\alpha}$.

As a final remark, the radius of maximum wind $R_{n,\alpha}$ ($n \in \{1,2\}$) appearing in the definition of Tilt (with α dropped) is defined to be the radius that maximises the φ -averaged azimuthal component of \mathbf{u}_n in a polar coordinate system whose origin is at the TC's rotational centre $\mathbf{x}_{n,\alpha}$ on level n .

Notes

1. Here and throughout this article, SCN refers to the condition in which the azimuthally averaged angular momentum and saturated pseudoadiabatic entropy contours are congruent.
2. A few tests suggested that adjusting the PDE for Π' to ensure $\partial_t(\nabla_h \cdot \mathbf{u}) = 0$ at $t=0$ in simulations with $f < 10^{-4} \text{ s}^{-1}$ causes no critical changes to the mature states of the system, which are the focus of this study.
3. Qualitatively similar behaviour for the time-dependence of V_{\max} was found with the same control parameters

($T_s = 32^\circ\text{C}$ and $f = 10^{-4} \text{ s}^{-1}$) using an independent cloud model (CM1) maintained by Dr. George Bryan at the Mesoscale & Microscale Meteorology Division of the National Centre for Atmospheric Research (Boulder, CO, USA). The model was configured to use the NASA-Goddard LFO microphysics parameterisation with graupel for the large ice category (cf. Lin et al., 1983). The complimentary NASA-Goddard long-wave and short-wave radiation module was also activated. The surface fluxes were parameterised using Deacon's formula, Rayleigh damping was applied above 17.5 km, and (unlike the RAMS simulation) a dissipative heating term was included in the thermodynamic energy equation. The grid resolution was comparable to that used here.

4. Note that the prefactor T_s/T_0 appearing in BR09b has been removed from the right-hand sides of eqs. (3) and (5) for consistency with the version of RAMS used for this study, which does not include dissipative heating (cf. Bister and Emanuel, 1998). Furthermore, estimating T_0 from properties of the DAS slightly differs from the BR09b practice of using the exact outflow temperature of air parcels passing through (r_{\max}, z_{\max}) .
5. Despite the extended range of the maximisation operator in the denominator, the operands in both parts of the fraction defining $\delta\sigma$ generally have maxima at radii less than $1.5R_0$. Recall that R_0 is the radius at which the boundary layer wind speed \bar{v}_0 is maximised.
6. The last paragraph of section 5.1 describes other distinguishing features of the lower simulations in Fig. 9a that may justify their separate consideration.
7. As one might infer from the tight correlation between $\delta\sigma$ and δKE_w seen in Fig. 8b, the latter measure of bulk updraft asymmetry is comparable to $\delta\sigma$ in its superior status as a statistical predictor of V_{\max}/V_{th} . A measure of the lower tropospheric updraft asymmetry δw is considered here instead of δKE_w to help show that not all measures of asymmetry are equally useful.
8. An alternative measure of the lower-middle tropospheric moist-entropy deficit is given by $\tilde{\chi} \equiv (s_{m*} - s_m)/(s_{s*} - s_s)$, in which s_s and s_{s*} are the actual and saturation entropies just above the sea surface. Previous studies have shown that the parameter $\tilde{\chi}$ (or some close analogue) can be useful for quantifying the variability of TC genesis rates, intensification rates and steady-state intensities, especially if the ambient wind shear is non-negligible (Rappin et al., 2010; Tang, 2010; Emanuel, 2010; DeMaria et al., 2012; Tang and Emanuel, 2012). Replacing χ with $\tilde{\chi}$ in this study does not appear to have any great benefit.

References

- Bell, M., Montgomery, M. T. and Emanuel, K. E. 2012. Air–sea enthalpy and momentum exchange at major hurricane wind speeds observed during CBLAST. *J. Atmos. Sci.* **69**, 3197–3222.

- Bister, M. and Emanuel, K. A. 1998. Dissipative heating and hurricane intensity. *Meteorol. Atmos. Phys.* **65**, 233–240.
- Black, P. G., D'Asaro, E. A., French, J. R., Drennan, W. M., French, J. R. and co-authors. 2007. Air–sea exchange in hurricanes: synthesis of observations from the coupled boundary layer air–sea transfer experiment. *Bull. Am. Meteorol. Soc.*, **88**, 357–374.
- Braun, S. A. and Tao, W.-K. 2000. Sensitivity of high-resolution simulations of hurricane Bob (1991) to planetary boundary layer parameterizations. *Mon. Weather Rev.* **128**, 3941–3961.
- Bryan, G. 2008. On the computation of pseudoadiabatic entropy and equivalent potential temperature. *Mon. Weather Rev.* **136**, 5239–5245.
- Bryan, G. 2012a. Effects of surface exchange coefficients and turbulence length scales on the intensity and structure of numerically simulated hurricanes. *Mon. Weather Rev.* **140**, 1125–1143.
- Bryan, G. 2012b. Comments on “Sensitivity of tropical-cyclone models to the surface drag coefficient.” *Q. J. Roy. Meteorol. Soc.* doi: 10.1002/qj.2066.
- Bryan, G. and Rotunno, R. 2009a. The maximum intensity of tropical cyclones in axisymmetric numerical model simulations. *Mon. Weather Rev.* **137**, 1770–1789.
- Bryan, G. and Rotunno, R. 2009b. Evaluation of an analytical model for the maximum intensity of tropical cyclones. *J. Atmos. Sci.* **66**, 3042–3060.
- Camargo, S. J., Sobel, A. H., Barnston, A. G. and Emanuel, K. A. 2007. Tropical cyclone genesis potential index in climate models. *Tellus A*, **59**, 4428–4443.
- Chavas, D. R. and Emanuel, K. 2012. Equilibrium tropical cyclone size in an idealized state of a radiative convective equilibrium. *30th Conference on Hurricanes and Tropical Meteorology*, American Meteorology Society, 10C.4. Online at: <https://ams.confex.com/ams/30Hurricane/webprogram/Paper204770.html>
- Cotton, W. R., Pielke Sr. R. A., Walko, R. L., Liston, G. E., Tremback, C. J. and co-authors. 2003. RAMS 2001. Current status and future directions. *Meteorol. Atmos. Phys.* **82**, 5–29.
- DeMaria, M., Knaff, J. A., Schumacher, A. B. and Kaplan, J. 2012. Improving tropical cyclone rapid intensity change forecasts. *30th Conference on Hurricanes and Tropical Meteorology*, American Meteorology Society, 8B7. Online at: <https://ams.confex.com/ams/30Hurricane/webprogram/Paper204582.html>
- Emanuel, K. A. 1986. An air sea interaction theory for tropical cyclones. Part I: steady state maintenance. *J. Atmos. Sci.* **43**, 585–604.
- Emanuel, K. A. 1988. The maximum intensity of hurricanes. *J. Atmos. Sci.* **45**, 1143–1155.
- Emanuel, K. A. 1995. Sensitivity of tropical cyclones to surface exchange coefficients and a revised steady state model incorporating eye dynamics. *J. Atmos. Sci.* **52**, 3969–3976.
- Emanuel, K. A. 2010. Tropical cyclone activity downscaled from NOAA-CIRES reanalysis, 1908–1958. *J. Adv. Model. Earth Sys.* **2**, 1–12.
- Emanuel, K. A. and Nolan, D. S. 2004. Tropical cyclone activity and the global climate system. *26th Conference on Hurricanes and Tropical Meteorology*, Miami, FL, American Meteorology Society, 240–241.
- Emanuel, K. A. and Rotunno, R. 2011. Self-stratification of tropical cyclone outflow. Part I: implications for storm structure. *J. Atmos. Sci.* **68**, 2236–2249.
- Frank, W. M. and Ritchie, E. A. 2001. Effects of vertical shear on the intensity and structure of numerically simulated hurricanes. *Mon. Weather Rev.* **129**, 2249–2269.
- Held, I. M. and Zhao, M. 2008. Horizontally homogeneous radiative-convective equilibria at GCM resolution. *J. Atmos. Sci.* **65**, 2003–2013.
- Hill, G. E. 1974. Factors controlling the size and spacing of cumulus clouds as revealed by numerical experiments. *J. Atmos. Sci.* **31**, 646–673.
- Jordan, C. L. 1958. Mean soundings for the West Indies area. *J. Meteorol.* **15**, 91–97.
- Khairoutdinov, M. F. and Emanuel, K. 2012. The effects of aggregated convection in cloud-resolved radiative-convective equilibrium. *30th Conference on Hurricanes and Tropical Meteorology*, American Meteorology Society, 12C.6. Online at: <https://ams.confex.com/ams/30Hurricane/webprogram/Paper206201.html>
- Lilly, D. K. 1962. On the numerical simulation of buoyant convection. *Tellus*, **XIV**, 148–172.
- Lin, Y.-L., Farley, R. D. and Orville, H. D. 1983. Bulk parameterization of the snow field in a cloud model. *J. Clim. Appl. Meteorol.* **22**, 1065–1092.
- Louis, J. F. 1979. A parametric model of vertical eddy fluxes in the atmosphere. *Boundary Layer Meteorol.* **17**, 187–202.
- Mahrer, Y. and Pielke, R. A. 1977. A numerical study of the airflow over irregular terrain. *Beitrage zur Physik der Atmosphäre* **50**, 98–113.
- Malkus, J. S. and Riehl, H. 1960. On the dynamics and energy transformations in a steady-state hurricane. *Tellus*, **12**, 1–20.
- Montgomery, M. T., Bell, M. M., Aberson, S. D. and Black, M. 2006. Hurricane Isabel (2003). New insights into the physics of intense storms. Part I: mean vortex structure and maximum intensity estimates. *Bull. Am. Meteorol. Soc.* **87**, 1335–1347.
- Montgomery, M. T., Smith, R. K. and Nguyen, S. V. 2010. Sensitivity of tropical cyclone models to surface exchange coefficients. *Q. J. Roy. Meteorol. Soc.* **136**, 1945–1953.
- Ooyama, K. 1969. Numerical simulation of the life cycle of tropical cyclones. *J. Atmos. Sci.* **26**, 3–40.
- Ooyama, K. 1982. Conceptual evolution of theory and modeling of the tropical cyclone. *J. Meteorol. Soc. Japan*, **60**, 369–379.
- Persing, J. and Montgomery, M. T. 2003. Hurricane super-intensity. *J. Atmos. Sci.* **60**, 2349–2371.
- Persing, J., Montgomery, M. T., McWilliams, J. C. and Smith, R. K. 2013. Asymmetric and axisymmetric dynamics of tropical cyclones. *Atmos. Chem. Phys. Discuss.* **13**, 13323–13438.
- Rappin, E. D., Nolan, D. S. and Emanuel, K. A. 2010. Thermodynamic control of tropical cyclogenesis in environments of radiative-convective equilibrium with shear. *Q. J. Roy. Meteorol. Soc.* **136**, 1954–1971.
- Riemer, M., Montgomery, M. T. and Nicholls, M. E. 2010. A new paradigm for intensity modification of tropical

- cyclones: thermodynamic impact of vertical wind shear on the inflow layer. *Atmos. Chem. Phys.* **10**, 3163–3188.
- Riehl, H. 1963. Some relations between wind and thermal structure of steady state hurricanes. *J. Atmos. Sci.* **20**, 276–287.
- Rotunno, R. and Emanuel, K. A. 1987. An air-sea interaction theory for tropical cyclones: Part II. Evolutionary study using a nonhydrostatic axisymmetric numerical model. *J. Atmos. Sci.* **44**, 542–561.
- Schecter, D. A. 2010. Hurricane intensity in the Ooyama (1969) paradigm. *Q. J. Roy. Meteorol. Soc.* **136**, 1920–1926.
- Schecter, D. A. 2011. Evaluation of a reduced model for investigating hurricane formation from turbulence. *Q. J. Roy. Meteorol. Soc.* **137**, 155–178.
- Schecter, D. A. and Dunkerton, T. J. 2009. Hurricane formation in diabatic Ekman turbulence. *Q. J. Roy. Meteorol. Soc.* **135**, 823–838.
- Smagorinsky, J. 1963. General circulation experiments with the primitive equations. *Mon. Weather Rev.* **91**, 99–164.
- Smith, R. K., Montgomery, M. T. and Nguyen, S. V. 2009. Tropical cyclone spin-up revisited. *Q. J. Roy. Meteorol. Soc.* **135**, 1321–1335.
- Smith, R. K., Montgomery, M. T. and Vogl, S. 2008. A critique of Emanuel's hurricane model and potential intensity theory. *Q. J. Roy. Meteorol. Soc.* **134**, 551–561.
- Smith, R. K. and Thomsen, G. L. 2010. Dependence of tropical-cyclone intensification on the boundary-layer representation in a numerical model. *Q. J. Roy. Meteorol. Soc.* **136**, 1671–1685.
- Tang, B. 2010. Mid-level ventilation's constraint on tropical cyclone intensity. PhD Dissertation. Massachusetts Institute of Technology, Cambridge, MA, USA, 195 pp.
- Tang, B. and Emanuel, K. 2010. Mid-level ventilation's constraint on tropical cyclone intensity. *J. Atmos. Sci.* **67**, 1817–1830.
- Tang, B. and Emanuel, K. 2012. A ventilation index for tropical cyclones. *Bull. Am. Meteorol. Soc.* **93**, 1901–1912.
- Velden, C., Harper, B., Wells, F., Beven II, J. L., Zehr, R. and co-authors. 2006. The Dvorak tropical cyclone intensity estimation technique. A satellite-based method that has endured for over 30 years. *Bull. Am. Meteorol. Soc.* **87**, 1195–1210.
- Walko, R. L., Band, L. E., Baron, J., Kittel, T. G. F., Lammers, R. and co-authors. 2000. Coupled atmosphere-biophysics-hydrology models for environmental modeling. *J. Appl. Meteorol.* **39**, 931–944.
- Walko, R. L., Cotton, W. R., Meyers, M. P. and Harrington, J. Y. 1995. New RAMS cloud microphysics parameterization. Part 1: the single-moment scheme. *Atmos. Res.* **38**, 29–62.
- Yang, B., Wang, Y. and Wang, B. 2007. The effect of internally generated inner-core asymmetries on tropical cyclone potential intensity. *J. Atmos. Sci.* **64**, 1165–1188.